Materials Advances

ROYAL SOCIETY OF CHEMISTRY

PAPER

View Article Online
View Journal | View Issue



Cite this: *Mater. Adv.*, 2025, 6, 7517

# Facile synthesis of $CoFe_2O_4$ powders for aqueous charge storage

M. R. Manei and S. M. Masoudpanah *

Received 3rd June 2025,
Accepted 31st August 2025

DOI: 10.1039/d5ma00583c

rsc.li/materials-advances

In this work, the electrochemical performance of $CoFe_2O_4$ powders was improved by selecting a proper organic fuel (glycine, urea, and citric acid) for the solution combustion synthesis method. Burning the glycine fuel led to the higher crystallinity, larger particle size, and spongy microstructure of the $CoFe_2O_4$ powders, caused by its high combustion temperature and combustion rate. In contrast, using urea and citric acid fuels resulted in higher specific surface areas of 57 and 47 $m^2\ g^{-1}$, respectively, than that (23 $m^2\ g^{-1}$) obtained using the glycine fuel due to the lower combustion temperature. The glycine-assisted $CoFe_2O_4$ powders exhibited high electrochemical performance, including high specific capacitances of 718 and 446 F $g^{-1}$ at current densities of 1 and 20 A $g^{-1}$, respectively. Furthermore, the asymmetric aqueous capacitor of $CoFe_2O_4$//activated carbon electrochemically stored an energy density of 42 Wh $kg^{-1}$ for the potential window of 0–1.5 V.



## 1. Introduction

Clean and renewable energy technologies have attracted significant attention for resolving the challenges of the shortage of fossil fuel resources and environmental pollution.[1] The development of energy storage and conversion devices, including supercapacitors, lithium-ion batteries, and fuel cells, has become an essential task for applying renewable energy resources such as hydropower, solar, wind, geothermal, and tidal energy due to their intermittent nature.[2–4] Remarkably, supercapacitors (SCs) can release energy faster for longer cycles based on the charge storage mechanism, making them suitable for hybrid electric vehicles (HEVs), wind turbines, and MP3 players.[5,6] Generally, there are two types of SCs:[7,8] electrical double-layer capacitors (EDLCs) and pseudocapacitors.[9,10] Electric double-layer electrodes physically adsorb charges on the electrode/electrolyte interface. Carbon active materials, carbon fibers, carbon nanotubes, and reduced graphene oxides, as carbon-derived materials with high specific surface areas, are typical electroactive materials used in EDLCs.[1,11,12] In contrast, pseudocapacitors store charges *via* fast, reversible oxidation/reduction reactions, sharing the electrons between the electroactive materials and the electrolyte. Pseudocapacitors have higher specific capacitance and energy density than EDLCs because of the nature of faradaic redox reactions.[13,14]

Various oxide, sulfide, phosphide, and nitride materials are used as pseudocapacitive materials. Among them, the binary metallic sulfides and nitrides have higher electrical conductivity and electrochemical performance. However, oxide materials are easily prepared and exhibit higher chemical stability.[15–17] Recently, mixed metal oxides (*e.g.* $NiCo_2O_4$, $ZnCo_2O_4$, $NiFe_2O_4$, and $CoFe_2O_4$) have been the subject of much research for pseudocapacitors because of their eco-sustainability, easy fabrication, and high specific capacitance.[18,19] Among them, the cobalt spinel ferrite ($CoFe_2O_4$) is applied for supercapacitors and Li-ion batteries due to its excellent electrochemical performance, low cost, and environmental friendliness.[20,21] For example, Song *et al.*[22] directly synthesized $CoFe_2O_4$ particles with hollow skeleton nanobox morphology on nickel foam by a green chemistry method, showing a high specific capacitance of 845 F $g^{-1}$. Gao *et al.*[23] synthesized the $CoFe_2O_4$ electrode with a high specific capacitance of 1342 F $g^{-1}$ at 1 A $g^{-1}$ by adding various surfactants during the hydrothermal method. Guo *et al.*[24] studied the electrochemical performance of the $CoFe_2O_4$ quantum dots prepared by the solvothermal method in various solvents. They reported outstanding electrochemical properties such as the largest initial specific capacitance of 1269 F $g^{-1}$ at 12 A $g^{-1}$. However, these methods are relatively complicated, time-consuming, and require expensive instruments.[25,26] Therefore, it is necessary to propose an easy, adoptable, scalable, and highly time- and energy-efficient method for synthesizing the $CoFe_2O_4$ material.

In this work, the $CoFe_2O_4$ powders were prepared by the solution combustion method, a convenient method in industry due to its fast kinetics and low cost.[27] Furthermore, the high porosity and high specific surface area caused by the evolution of gases are unique characteristics of the combusted products.[28,29] The microstructural and electrochemical properties of the combusted products are adjustable by the type and amount of metal precursor as oxidant and organic compounds as fuels. Here, the

*School of Metallurgy and Materials Engineering, Iran University of Science and Technology (IUST), Tehran, Iran. E-mail: masoodpanah@iust.ac.ir*

effects of fuel type (*e.g.* urea, glycine, and citric acid) were studied by various characterization methods. The $CoFe_2O_4$ powders have been prepared by the SCS method using glycine, urea, and citric acid as organic fuel for magnetic and biomedical applications. However, the effects of fuel type can be different on the charge storage performance because the electrochemical properties are strongly dependent on the physicochemical properties of the particles' surface.[30–32] In other words, the novelty of our work is based on the systematic study of the role of fuel type on the electrochemical performance of $CoFe_2O_4$ powders.

## 2. Experimental procedure

The metal precursors, including $Fe(NO_3)_3{\cdot}9H_2O$ and $Co(NO_3)_2{\cdot}6H_2O$, and organic fuels such as citric acid ($C_6H_8O_7$), glycine ($C_2H_5NO_2$), and urea ($CO(NH_2)_2$), were purchased from Merck Company.

### 2.1. Synthesis method

Typically, 1 mmol of $Co(NO_3)_2{\cdot}6H_2O$ and 2 mmol of $Fe(NO_3)_3{\cdot}9H_2O$ were dissolved in 30 mL of distilled water as solvent. The citric acid, glycine, and urea as fuels were then added to the precursor solution. The amounts of fuel were calculated based on the following reactions (eqn (1)–(3)):[29,33]

$$Co(NO_3)_2{\cdot}6H_2O + 2Fe(NO_3)_3{\cdot}9H_2O + \frac{20\varphi}{9}C_6H_8O_7 + 10(\varphi-1)O_2 \rightarrow CoFe_2O_4 + \frac{40\varphi}{3}CO_2 + \left(24+\frac{80\varphi}{9}\right)H_2O + 4N_2 \quad (1)$$

$$Co(NO_3)_2{\cdot}6H_2O + 2Fe(NO_3)_3{\cdot}9H_2O + \frac{40\varphi}{9}C_2H_5NO_2 + 10(\varphi-1)O_2 \rightarrow CoFe_2O_4 + \frac{80\varphi}{9}CO_2 + \left(24+\frac{100\varphi}{9}\right)H_2O + \left(4+\frac{20\varphi}{9}\right)N_2 \quad (2)$$

$$Co(NO_3)_2{\cdot}6H_2O + 2Fe(NO_3)_3{\cdot}9H_2O + \frac{40\varphi}{6}CH_4N_2O + 10(\varphi-1)O_2 \rightarrow CoFe_2O_4 + \frac{40\varphi}{6}CO_2 + \left(24+\frac{40\varphi}{3}\right)H_2O + \left(4+\frac{40\varphi}{6}\right)N_2 \quad (3)$$

The fuel-to-oxidant ratio ($\varphi$) shows the required amounts of external oxygen. The $\varphi$ value was set to 1.5. The precursor solution was heated at 80 °C to evaporate the solvent. The dried gels were ignited on a hot plate by increasing the temperature up to 250 °C. The self-propagating exothermic reaction started from a point and proceeded without providing any external energy. The combusted products were manually crushed and were calcined at 450 °C for 1 hour in an air atmosphere. The powders were coded according to the fuel type; for example, the powders prepared by the glycine fuel were shown by the "G" symbol.

### 2.2. Materials characterization methods

The structure and phase of the powders were analyzed by X-ray diffractometry (D8 ADVANCE, Bruker, Kanagawa, Japan) by using Cu Kα irradiation ($\lambda$ = 0.154 nm) generated by an accelerating voltage of 40 kV and a current of 30 mA. The powders were scanned in the diffraction range of $2\theta$ = 10–80° with a scan rate of 0.05°/1 s. The microstructure was examined using scanning electron microscopy (Vega II, TESCAN, Czech Republic) and transmission electron microscopy (PHILIPS CM-300). The $N_2$ ad/desorption isotherms were obtained from the degassed powders at 250 °C for 5 h to calculate the BET specific surface area and pore size distribution plot.

### 2.3. Electrochemical measurement

**2.3.1. Three-electrode system.** The nickel foams (1 × 3 $cm^2$) as substrates were immersed in 3 M HCl solution, 3 M NaOH solution, ethanol, and distilled water, respectively, to remove organic pollutants and oxide layers.

To prepare the working electrode, firstly, 5 wt% polyvinylidene fluoride as a binder was dissolved in about 1 ml *N*-methyl-2-pyrrolidone solvent. Then, 15 wt% carbon black and 80 wt% electroactive powders were dispersed in the binder solution. The coated nickel foam was dried at 80 °C for 24 h, leading to a mass loading of 1 mg $cm^{-2}$.

Electrochemical properties were analyzed by cyclic voltammetry (CV), galvanostatic charge/discharge (GCD), and electrochemical impedance spectroscopy techniques on the Radstat 10 (Kianshardanesh, Iran) instrument. The electrochemical performance of the working electrode was evaluated in a three-electrode system including Ag/AgCl and Pt wire as reference and counter electrodes, respectively, and 3 M KOH solution as electrolyte. The CV curves were obtained at various scan rates of 5, 10, 20, 30, 40, and 50 mV $s^{-1}$ in the potential range of 0–0.5 V *vs.* Ag/AgCl. The specific capacitance ($C_{sp}$) was calculated by the area of CV curves as follows (eqn (4)):[34]

$$C_{sp} = \frac{\int i\mathrm{d}v}{2m\vartheta\Delta V} \quad (4)$$

where m, $\Delta V$, and $\nu$ are loading mass, potential window, and scan rate, respectively. The GCD tests were performed in various current densities of 1, 2, 3, 4, 5, 10, and 20 A $g^{-1}$. The specific capacitance ($C_{sp}$) was obtained by eqn (5):[35]

$$C_{sp} = \frac{I\Delta t}{m\Delta V} \quad (5)$$

where $I$ and $\Delta t$ are constant current and discharge time, respectively. Electrochemical impedance spectroscopy (EIS) was also performed in the frequency range of 0.01 Hz to 50 kHz.

**2.3.2. Two-electrode system.** The asymmetric capacitor was fabricated by using the G powders and activated carbon (AC) as positive and negative electrodes, respectively. The electrolyte and separator were 3 M KOH solution and a filter paper. For balancing the positive and negative charges and preventing the electrode polarization, their loading mass should be adjusted according to the following equation by using specific capacitance ($C_{s\pm}$) and potential windows ($\Delta V_{\pm}$) of negative and

positive electrodes in a three-electrode system (eqn (6)):[36]

$$\frac{m_+}{m_-} = \frac{C_{s-} \cdot (\Delta V)_-}{C_{s+} \cdot (\Delta V)_+} \quad (6)$$

The energy density and power density of $CoFe_2O_4$//AC capacitor can be calculated from the specific capacitance ($C_s$), potential window ($\Delta V$), and discharge time ($\Delta t$) as follows (eqn (7) and (8)):[37]

$$\text{Energy density (ED)} = \frac{C_s \Delta V^2}{2} \quad (7)$$

$$\text{Power density (PD)} = \frac{\text{ED}}{\Delta t} \quad (8)$$

The electrochemical tests were repeated three times on various electrodes, resulting in a relative uncertainty of 1%.

## 3. Results and discussion

### 3.1. Structural and microstructural characterization

XRD patterns of the powders synthesized by glycine (G), citric acid (CA), and urea (U) fuels are shown in Fig. 1a. The indexed reflections of (220), (311), (422), and (440) are related to the spinel structure of the $CoFe_2O_4$ phase with the space group of *Fd*3*m*. There are no extra diffraction peaks, indicating the phase purity of the powders. The G powders show sharp and intense peaks due to their high crystallinity. However, the CA and U samples exhibit noisy patterns with broad diffraction peaks, which are attributed to their smaller crystallite size and higher crystal defects. The combustion reaction starts by the thermal decomposition of metal nitrates to the corresponding oxides as follows (eqn (9) and (10)):[33]

$$Co(NO_3)_2 \rightarrow CoO + N_2 + 3O_2 \quad (9)$$

$$2Fe(NO_3)_3 \rightarrow \alpha\text{-}Fe_2O_3 + 3N_2 + 9O_2 \quad (10)$$

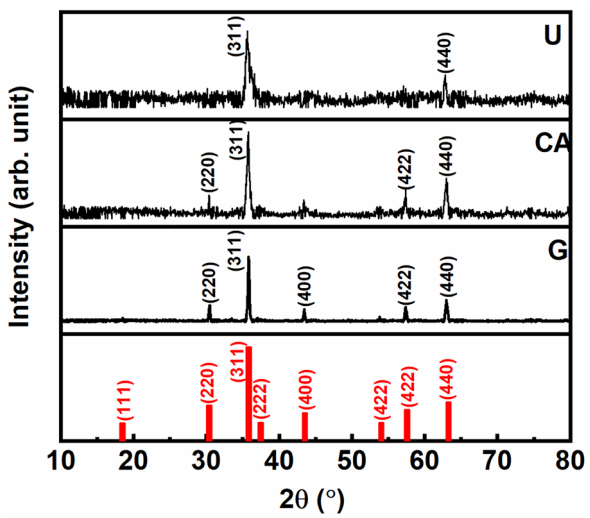


Fig. 1 XRD patterns of the powders prepared using glycine (G), citric acid (CA), and urea (U) fuels.

The released $O_2$ gas can simultaneously oxidize the fuel to liberate the heat and different gaseous products. The liberated thermal energy is utilized to proceed with the solid-state reaction between cobalt and ferric oxides to crystallize the cobalt ferrite as follows (eqn (11)):[38]

$$CoO + Fe_2O_3 \rightarrow CoFe_2O_4 \quad (11)$$

Therefore, the required heat for the solid-state reaction is provided by organic fuels, which depend on their bonding type, functional groups, and molecular structure, influencing the combustion temperature and combustion rate.[39] The glycine molecule, which has a carboxylic group and an amine group, exhibits a higher combustion rate and temperature. However, the citric acid fuel has only three carboxylic groups, and the urea molecule has two amine groups, leading to a slower combustion rate at lower combustion temperatures.[40] The higher crystalline $CoFe_2O_4$ powders with larger particles can be attributed to the higher combustion temperature obtained by glycine fuel.

SEM images of the G, CA, and U samples are presented in Fig. 2. The G samples are composed of spongy powders with large and crystalline $CoFe_2O_4$ particles; however, the bulky morphology with some small pores appears when using citric acid and urea fuels. The combustion microstructure is primarily related to the combustion rate, which liberates combustion gases and foams large powders. However, the higher combustion temperature promotes the particles' growth and sintering, closing up the pores between particles.[41] Therefore, the porous microstructure of the G powders can be attributed to the higher combustion rate. The large $CoFe_2O_4$ particles confirm the high combustion temperature developed by the glycine fuel. However, the slow burning of the citric acid and urea fuel leads to a few small pores. The smaller $CoFe_2O_4$ particles with lower crystallinity are due to the lower combustion temperature obtained by the urea fuel. The elemental maps of Fe, Co, and O and the EDS spectrum of the G powders are presented in Fig. 3. The uniform distribution of various elements indicates the phase purity without any segregation. Furthermore, the atomic ratio of Co/Fe is about 0.44, which is in agreement with the theoretical value (0.5).

Fig. 4 shows the TEM images and SAED patterns of the G, CA, and U samples. There are large cubic $CoFe_2O_4$ particles (~80 nm) that are tightly sintered together in the G powders. However, the particles are downsized up to ~40 and ~20 nm by using citric acid and urea fuels, respectively, due to the decrease in combustion temperature. Furthermore, there are numerous pores between the $CoFe_2O_4$ nanoparticles obtained using citric acid and urea fuels. The spot pattern of the G powders confirms the single-crystal nature of large particles. However, the indexed ring patterns of the U and CA samples further prove their nanostructured microstructure.

The $N_2$ ad/desorption isotherms and pore size distribution plots are presented in Fig. 5. The samples show the IV type isotherms with H3 hysteresis, indicating the fragile agglomeration of $CoFe_2O_4$ nanoparticles.[42] The BET specific surface area

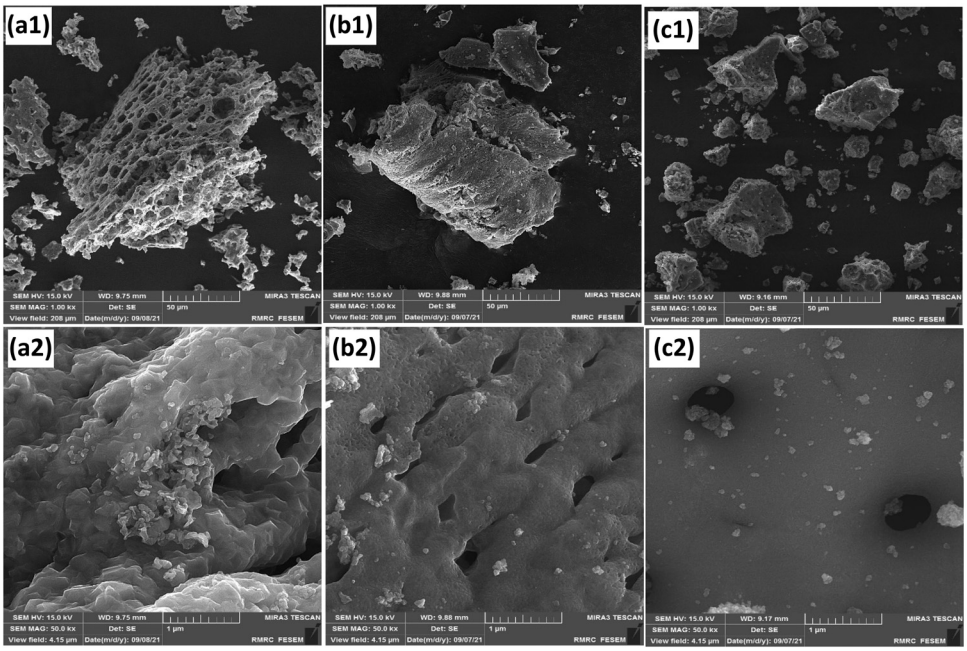


Fig. 2 SEM images of (a1) and (a2) G, (b1) and (b2) CA, and (c1) and (c2) U samples.

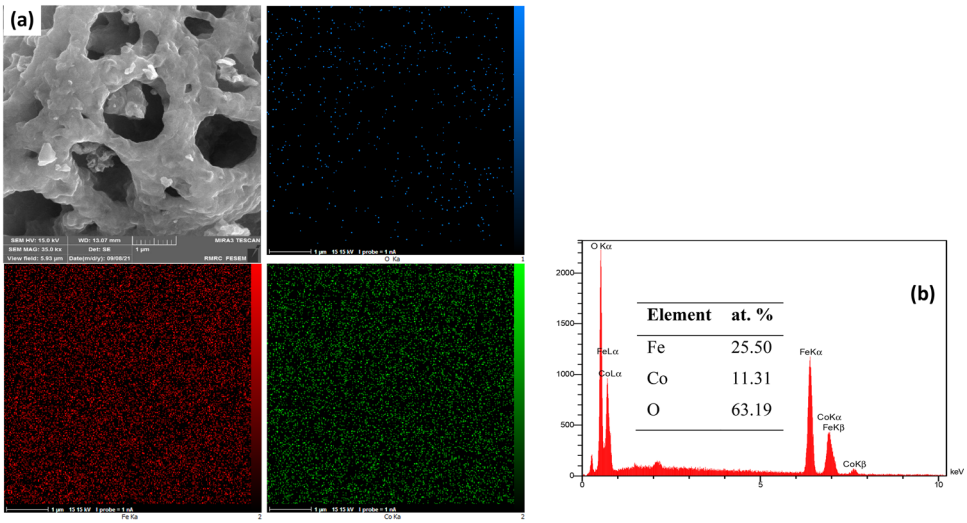


Fig. 3 (a) SEM image and elemental maps of the G sample, and (b) EDS spectrum of the G sample.

increases from 23 to 47 and 57 $m^2\ g^{-1}$ for the G, CA, and U samples, respectively. The higher specific surface area of the U sample can be attributed to its lower combustion temperature, preventing the particles' sintering and growth.[43] The pore size distribution plots show that there is a mixture of micropores (1–2 nm) and mesopores (2–50 nm). The CA and U samples have mainly mesopores of 4–5 nm (Fig. 4), which are responsible for their higher specific surface area. Furthermore, the pore volume indicates a similar trend; it increases from 0.06 to 0.16 and 0.19 $cm^3\ g^{-1}$ for the G, CA, and U samples, respectively. The higher pore volume of the U and CA samples can be attributed to the slow liberation of the gaseous products by the urea and citric acid fuels.

### 3.2. Electrochemical properties

**3.2.1. Three-electrode system.** Fig. 6a shows the cyclic voltammetry curves of the various G, CA, and U electrodes in the potential range of 0–0.45 V *vs.* Ag/AgCl at a scan rate of 5 mV $s^{-1}$. There are a pair of broad redox peaks for all samples, indicating their battery-type behavior. The reversible oxidation and reduction reactions between $CoFe_2O_4$ particles

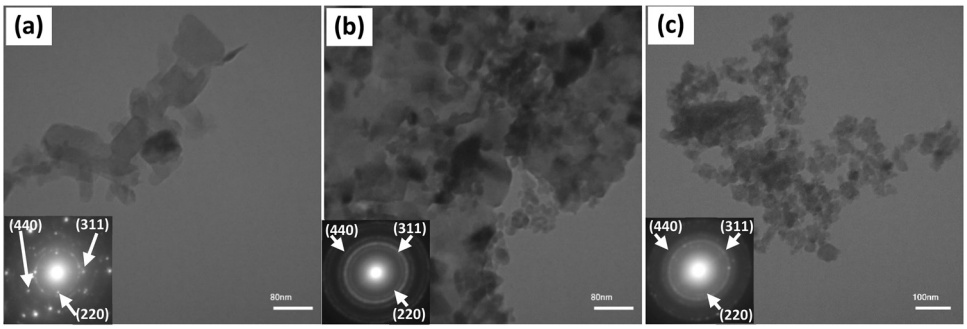


Fig. 4 TEM images and SAED patterns of (a) G, (b) CA, and (c) U samples.

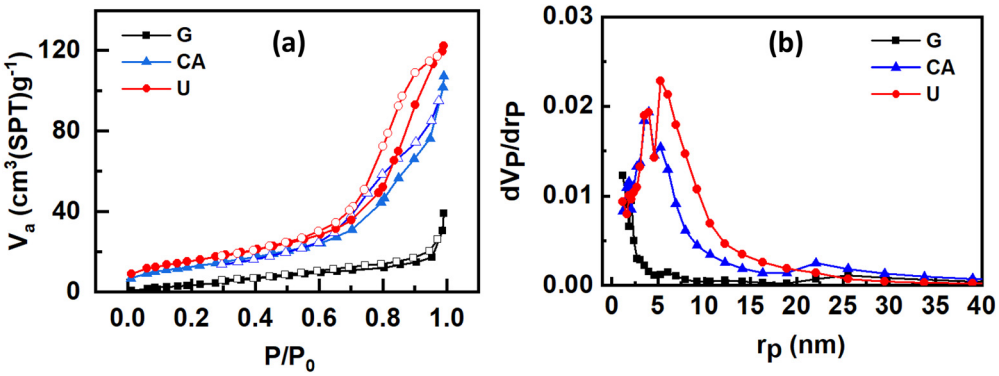


Fig. 5 (a) $N_2$ ad/desorption isotherms and (b) pore size distribution plots of the various samples.

and electrolyte ($OH^-$) ions during charging and discharging processes can be considered as follows (eqn (12)–(14)):[44]

$$CoFe_2O_4 + OH^- \leftrightarrow CoOOH + FeOOH + e^- \quad (12)$$

$$FeOOH + H_2O \leftrightarrow FeO + OH^- \quad (13)$$

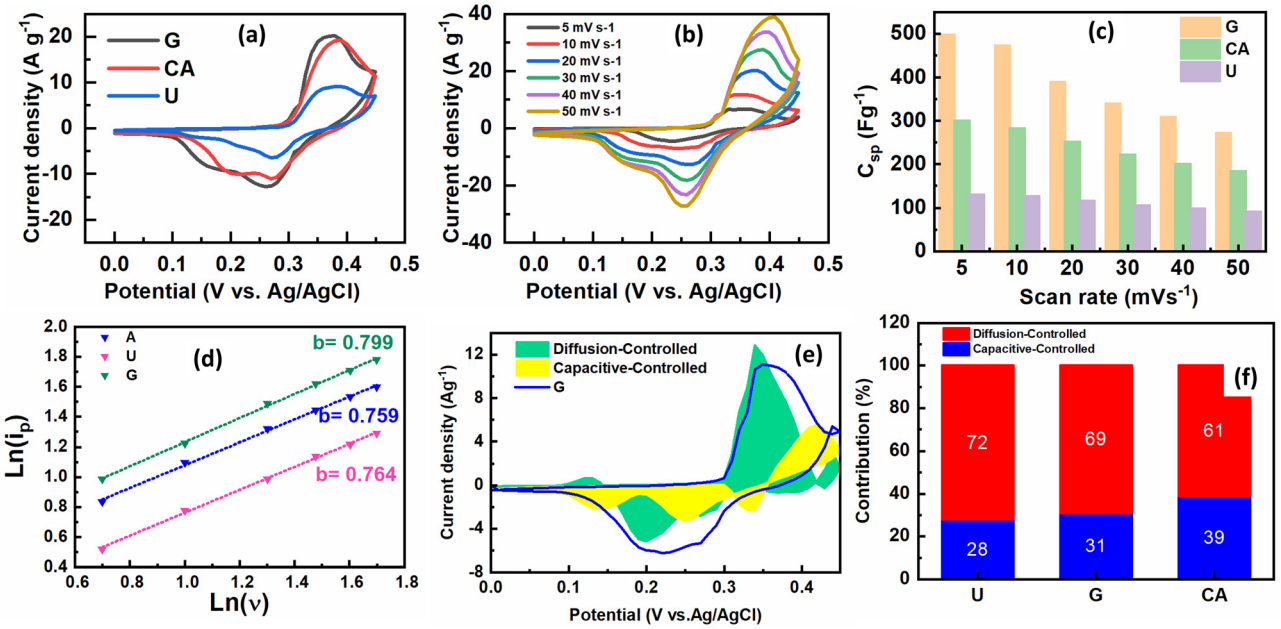


Fig. 6 (a) CV curves at a scan rate of 5 mV $s^{-1}$, (b) CV curves of the G electrode, (c) specific capacitance *versus* scan rate, (d) ln($i_p$) *vs.* ln(ν) plot, (e) capacitive- and diffusion-controlled CV curves, and (f) the contribution ratio of various electrodes.

$$CoOOH + OH^- \leftrightarrow CoO_2 + H_2O + e^- \quad (14)$$

Since the specific capacitance is proportional to the area enveloped by CV curves, the G electrode has a higher specific capacitance of 497 F $g^{-1}$, which decreases up to 300 and 130 F $g^{-1}$ for the CA and U samples, respectively. With the increase of scan rate (Fig. 6b), the anodic and cathodic peaks are separated from each other, and the current response increases due to the insufficient time for redox reactions at the higher scan rates. Fig. 6c shows the dependence of specific capacitance on the scan rate. The G electrode has a higher specific capacitance than other electrodes at all scan rates due to its higher crystallinity, leading to higher electrical conductivity for sharing electrons with electrolyte ($OH^-$) ions. With the increase of scan rate from 5 to 50 mV $s^{-1}$, the specific capacitance of the G electrode decreases from 497 to 272 F $g^{-1}$. The Faradaic and capacitive mechanisms can be analyzed using the power law: $i = a\nu^b$, where the $b$ value of 0.5 indicates reversible redox reactions for electron exchange, and the $b$ value of 1 is associated with the capacitive mechanism (non-faradaic mechanism). The $b$ value can be calculated as the slope of the $\ln(i_p)$ *vs.* $\ln(\nu)$ plots (Fig. 6d). The $b$ value of 0.75–0.8 further proves the battery-type behavior of various electrodes. The contribution ratio of various capacitive-controlled ($k_1\nu$) and diffusion-controlled ($k_2\nu^{0.5}$) mechanisms can be analyzed by considering their superposition of current responses as follows:[34]

$$i(V) = k_1\vartheta + k_2\vartheta^{0.5} \quad (15)$$

By plotting $\frac{i}{\vartheta^{0.5}}$ *vs.* $k_1\vartheta^{0.5} + k_2$, the $k_1$ and $k_2$ coefficients are calculated for determining the current responses of the capacitive- and diffusion-controlled mechanisms. The current responses of various mechanisms are illustrated in Fig. 6e for the G electrode. The trend of contribution ratio on the fuel type is presented in Fig. 6f. The diffusion-controlled contribution decreases from 72 to 69% and 61% for the U, G, and CA samples, respectively.

Fig. 7a compares the GCD curves of the G, CA, and U electrodes at a current density of 1 A $g^{-1}$. There is a pair of voltage plateaus on the charge and discharge curves, confirming the battery-type behavior. The longer the discharging time, the higher the specific capacitance. Therefore, the G electrode has a higher specific capacitance of 718 F $g^{-1}$ than that of 428 and 270 F $g^{-1}$ for the CA and U electrodes, respectively. The dependence of GCD curves on the current density for the G sample is shown in Fig. 7b. Although the voltage plateaus shrink at the higher current densities, there are stable plateaus, indicating the high electrochemical stability. The G electrode has the specific capacitance of 718, 670, 652, 627, 605, 514, and 446 F $g^{-1}$ at various current densities of 1, 2, 3, 4, 5, 10, and 20 A $g^{-1}$. The dependence of specific capacitance *versus* current density is summarized in Fig. 7c. The G sample has the highest specific capacitance at all current densities. The capability rate of the G electrode is 62%, while it decreases up to 57% and 34% for the CA and U electrodes, respectively. In other words, the G electrode shows the higher retainability of specific capacitance on account of its higher crystallinity of combusted $CoFe_2O_4$ powders. The capability rate of the various electroactive materials is compared in

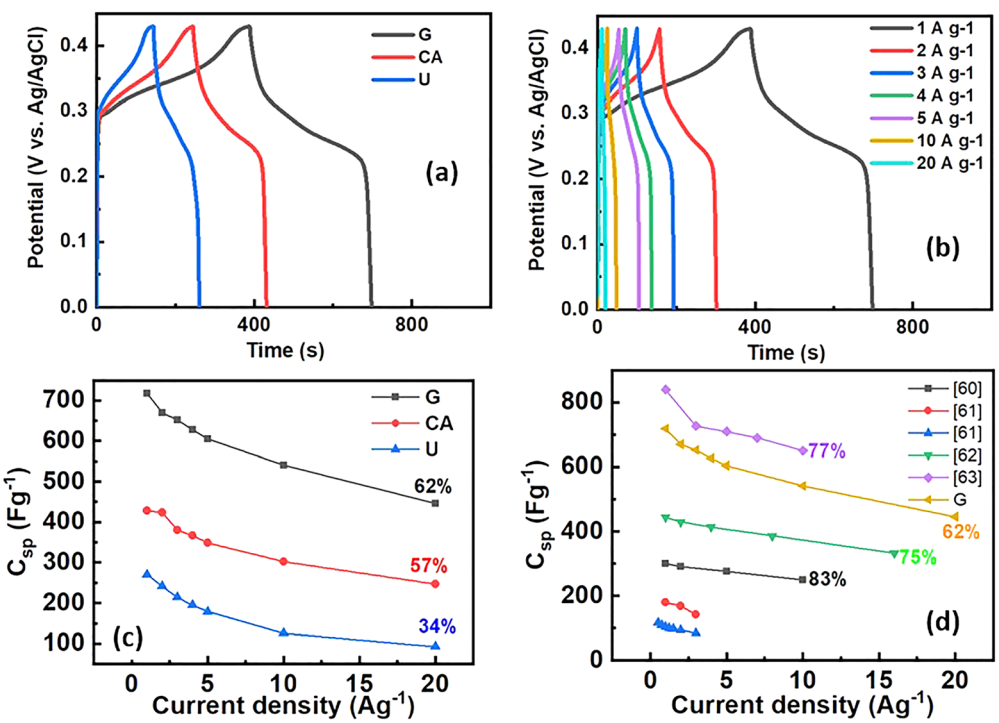


Fig. 7 (a) GCD curves at a current density of 1 A $g^{-1}$, (b) GCD curves of the G sample, (c) specific capacitance *vs.* current density, and (d) comparison of the capability rate with other reported works.[45–48]

Fig. 7d. The G electrode shows the lowest capability rate of 62%, maybe due to its larger particle size. However, the higher specific capacitance of the G electrode can be attributed to its higher crystallinity caused by the high synthesis temperature developed by the exothermic combustion reaction. Furthermore, the synthesis method is simpler and a more time- and energy-efficient technique in comparison with other synthesis methods for the preparation of complicated compounds for storage and conversion in electrochemical systems.

The electrochemical reaction kinetics of the electroactive materials can be evaluated by the electrochemical impedance spectroscopy (EIS) technique, which is presented by the Nyquist plots ($-Z''$ *vs.* $Z'$) (Fig. 8a). The Nyquist plots are composed of a semicircle and an inclined line in high- and low-frequency regions, respectively. The $Z'$ intercept in the high-frequency region shows the total inner ($R_s$) resistance of the electrode. The diameter of the semicircle is related to the charge transfer resistance ($R_{ct}$) at the electrode and electrolyte interface. The diffusion of electrolyte ions into the electrode structure leads to an inclined linear, as Warburg impedance. The fitted values of $R_s$, $R_{ct}$, and $W_o$, calculated using the presented equivalent circuit, are summarized in Fig. 8b. The various electrodes have similar solution resistance in the range of 1.5 Ω. The G electrode shows the lowest charge transfer resistance (Rct) of 3.128 Ω, which increases up to 9.25 Ω for the CA electrode. The higher electrochemical kinetics of the G electrode can be attributed to the higher crystallinity, which promotes higher electrical conductivity (Fig. 8).

Finally, the glycine fuel as an amino acid with chelatability is relatively expensive (10–20 USD $kg^{-1}$) but offers higher product purity and charge storage capability. Burning glycine results in fewer toxic residues. The lower electrochemical properties are obtained by the citric acid fuel, but its cost (2–5 USD $kg^{-1}$) is lower than that of glycine but comparable to that of urea fuel. The citric acid exhibits biodegradability and low toxicity. The urea fuel is an inexpensive organic compound (0.5–1 USD $kg^{-1}$) with minimal toxic residues, making it attractive for large-scale synthesis. However, the urea-assisted sample exhibits a lower charge storage capability.[29,38]

**3.2.2. Two-electrode system.** The practical application of G powders can be evaluated by assembling an aqueous asymmetric supercapacitor (ASC) device. The G powders and activated carbon (AC) were applied as positive and negative electrodes, respectively, due to their practical potential windows in a three-electrode system, as presented in Fig. 9a. It is expected that the $CoFe_2O_4$//AC capacitor has a practical potential window of 0–1.5 V because the G and AC electrodes have stable potential windows of 0–0.5 V and −1 to 0 V *vs.* Ag/AgCl, respectively. However, the operating window of the CoFe2O4//AC capacitor can be determined by evaluating the CV and GCD curves at various potential windows from 0–1 V to 0–1.6 V, as shown in Fig. 9b and c. Gas bubbles are released from the assembled cell at a potential window of 0–1.6 V. For a potential window of 0–1.4 V, there is no water splitting and overcharging in the CV and GCD curves. Therefore, the $CoFe_2O_4$//AC capacitor can operate stably and safely in the potential window of 0–1.4 V without any electrolyte decomposition and current leakage. The $CoFe_2O_4$//AC capacitor shows a pair of broad redox peaks (Fig. 9d) without any significant distortion at high scan rates, indicating the high reversibility of the $CoFe_2O_4$ electrode caused by its higher crystallinity and porous microstructure. The mesoporous structure of the as-combusted $CoFe_2O_4$ powders is favorable for charge and ionic transfer inside the electrode. The triangular shape of GCD curves with a negligible IR drop during the discharge (Fig. 9e) shows capacitive behavior with low internal resistance of the assembled $CoFe_2O_4$//AC capacitor. The $CoFe_2O_4$//AC device can store a relatively high specific capacitance of 137 F $g^{-1}$ at a current density of 1 A $g^{-1}$, which corresponds to the energy density of 42 Wh $kg^{-1}$ at a power density of 750 W $kg^{-1}$ at current densities of 1 and 20 A $g^{-1}$, respectively. The assembled $CoFe_2O_4$//AC capacitor can be powered to light up the various LED lamps for 4 minutes (Fig. 9f). The cycling performance of the G//AC capacitor was evaluated at 5 A $g^{-1}$ for 3500 charge and discharge cycles (Fig. 9g). The capacitance retention is 84.6%. The acceptable electrochemical performance of the $CoFe_2O_4$//AC device is attributed to the higher crystallinity and porous structure of the $CoFe_2O_4$ powders prepared by glycine fuel.

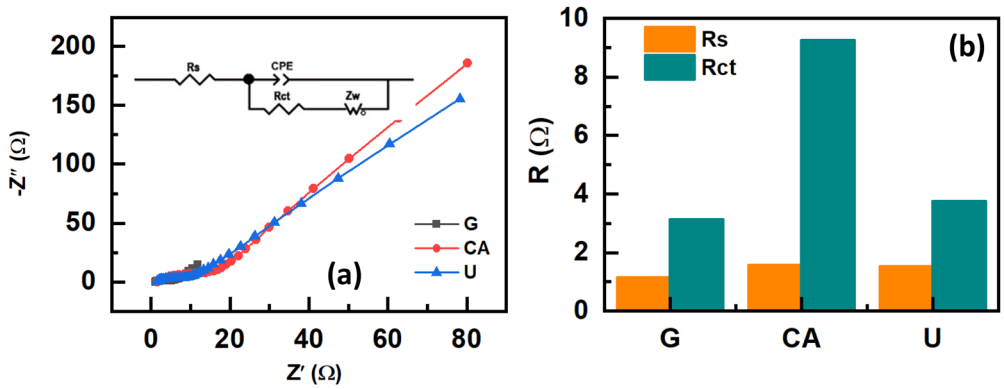


Fig. 8 (a) Nyquist plots and equivalent circuit, and (b) the fitted values of solution resistance ($R_s$) and charge transfer resistance ($R_{ct}$) of the various electrodes.

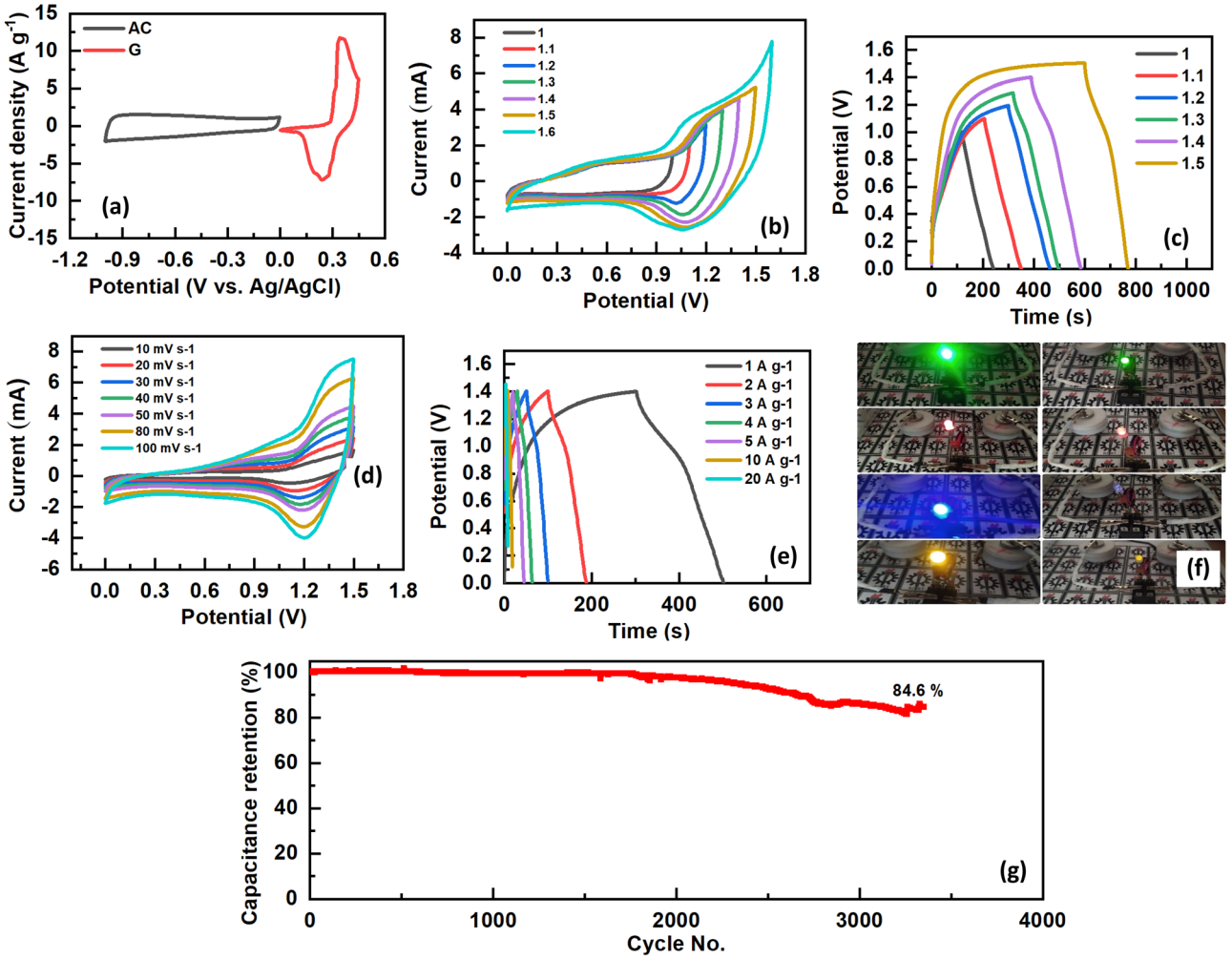


Fig. 9 (a) CV curves of the $CoFe_2O_4$ and AC electrodes in a three-electrode system at a scan rate of 5 mV $s^{-1}$, (b) CV curves of the $CoFe_2O_4$//AC capacitor at a scan rate of 20 mV $s^{-1}$ and (c) GCD curves of the $CoFe_2O_4$//AC capacitor at a current density of 1 A $g^{-1}$, (d) CV and (e) GCD curves, (f) lighting up of two LED lamps by serially connected two $CoFe_2O_4$//AC capacitors, and (g) cycling performance at 5 A $g^{-1}$.

## 4. Conclusion

Single-phase $CoFe_2O_4$ powders with various crystallinity, microstructure, and electrochemical performance were prepared by the solution combustion synthesis method using different organic fuels. The glycine fuel led to high crystallinity and foamy microstructure with large pores due to its high combustion temperature. Although the glycine-assisted $CoFe_2O_4$ powders had a lower specific surface area, they exhibited a higher charge storage capability, including a specific capacitance of 718 F $g^{-1}$ at a current density of 1 A $g^{-1}$, which decreased up to 446 F $g^{-1}$ at 20 A $g^{-1}$. Furthermore, the $CoFe_2O_4$ powders prepared by glycine fuel were used as a positive electrode for assembling an asymmetric aqueous capacitor with activated carbon as a negative electrode. The capacitor electrochemically stores an energy density of 42 Wh $kg^{-1}$ for the potential window of 0–1.5 V.

## Conflicts of interest

There are no conflicts to declare.

## Data availability

The datasets used and/or analysed during the current study are available from the corresponding author on reasonable request.

## References

1 K. A. A. A. Elsehsah, Z. A. Noorden and N. M. Saman, *J. Energy Storage*, 2024, **97**, 112788.
2 M. F. Ponce, A. Mamani, P. B. Ramos, F. Jerez, G. G. Acosta, J. E. Tasca and M. A. Bavio, *Front. Chem. Sci. Eng.*, 2025, **19**, 62.
3 D. Lemian and F. Bode, *Energies*, 2022, **15**, 5683.
4 A. Daghouri, S. El Hani, Y. El Hachimi and H. Mediouni, *Results Eng.*, 2024, **23**, 102634.
5 J. Zhang, M. Gu and X. Chen, *Micro Nano Eng.*, 2023, **21**, 100229.
6 K. O. Oyedotun and B. B. Mamba, *Inorg. Chem. Commun.*, 2024, **170**, 113154.

7 W. Pholauyphon, P. Charoen-amornkitt, T. Suzuki and S. Tsushima, *J. Energy Storage*, 2024, **98**, 112833.
8 S. Sharma and P. Chand, *Results Chem.*, 2023, **5**, 100885.
9 K. C. S. Lakshmi and B. Vedhanarayanan, *Batteries*, 2023, **9**(4), 202.
10 J. Theerthagiri, S. J. Lee, P. Shanmugam and M. Y. Choi, in *Nanostructured, Functional, and Flexible Materials for Energy Conversion and Storage Systems*, ed. A. Pandikumar and P. Rameshkumar, Elsevier, 2020, pp. 1–14, DOI: 10.1016/B978-0-12-819552-9.00001-4.
11 M. E. Şahin, F. Blaabjerg and A. Sangwongwanich, *Energies*, 2022, **15**(3), 674.
12 J. M. Lim, Y. S. Jang, H. Van, T. Nguyen, J. S. Kim, Y. Yoon, B. J. Park, D. H. Seo, K.-K. Lee, Z. Han, K. Ostrikov and S. G. Doo, *Nanoscale Adv.*, 2023, **5**, 615–626.
13 H. W. Park and K. C. Roh, *J. Power Sources*, 2023, **557**, 232558.
14 H. Rashid Khan and A. Latif Ahmad, *J. Ind. Eng. Chem.*, 2025, **141**, 46–66.
15 H. Liu, X. Liu, S. Wang, H.-K. Liu and L. Li, *Energy Storage Mater.*, 2020, **28**, 122–145.
16 M. Liu, Y. Liu, B. Gu, X. Wei, G. Xu, X. Wang, M. T. Swihart and K.-T. Yong, *Chem. Soc. Rev.*, 2019, **48**, 4950–4965.
17 C. Huang, P. Qin, D. Li, Q. Ruan, H. Song, L. Liu, Y. Wu, Y. Ma, Q. Li, K. Huo and P. K. Chu, *J. Energy Chem.*, 2022, **69**, 561–568.
18 Y. Zhang, Y.-y Zhang, C.-e Li, X.-h Yan, S. Hu, R.-b Yin, Y.-f Wei, K.-z Gao and H.-l Gao, *Coord. Chem. Rev.*, 2024, **519**, 216103.
19 D. Malavekar, S. Pujari, S. Jang, S. Bachankar and J. H. Kim, *Small*, 2024, **20**, 2312179.
20 O. Baytar, A. Ekinci, Ö. Şahin and A. Akdag, *ChemistrySelect*, 2024, **9**, e202304491.
21 M. Ashan, H. A. Alyousef, A. W. Alrowaily, B. M. Alotaibi, N. Al-Harbi, H. H. Somaily, M. Aslam, K. Ahmad and S. Aman, *Electrochim. Acta*, 2024, **504**, 144840.
22 K. Song, R. Yang, X. Wang, B. Zhang, J. Wang and X. Chen, *Appl. Surf. Sci.*, 2020, **533**, 147433.
23 L. Gao, E. Han, Y. He, C. Du, J. Liu and X. Yang, *Ionics*, 2020, **26**, 3643–3654.
24 X. Guo, C. Yang, G. Huang, Q. Mou, H. Zhang and B. He, *J. Alloys Compd.*, 2018, **764**, 128–135.
25 B. Rani, A. K. Nayak and N. K. Sahu, *Diamond Relat. Mater.*, 2021, **120**, 108671.
26 J. Otabil Bonsu, A. B. Appiagyei and J. I. Han, *Mater. Res. Bull.*, 2021, **133**, 111053.
27 A. Varma, A. S. Mukasyan, A. S. Rogachev and K. V. Manukyan, *Chem. Rev.*, 2016, **116**, 14493–14586.
28 F. Deganello and A. K. Tyagi, *Prog. Cryst. Growth Charact. Mater.*, 2018, **64**, 23–61.
29 F. Siddique, S. Gonzalez-Cortes, A. Mirzaei, T. Xiao, M. A. Rafiq and X. Zhang, *Nanoscale*, 2022, **14**, 11806–11868.
30 D. Gogoi, P. Makkar, M. R. Das and N. N. Ghosh, *ACS Appl. Electron. Mater.*, 2022, **4**, 795–806.
31 V. S. Manikandan, T. Kavin Kumar, R. K. Poobalan, P. Sakthivel, N. Chidhambaram, N. Dineshbabu, S. S. Dhanabalan, C. V. Abarzúa, M. J. Morel and A. Thirumurugan, *J. Mater. Sci.: Mater. Electron.*, 2024, **35**, 46.
32 A. Ghazal, A. C. Mendhe, A. Kore, S. Dhas, R. Batool and D. Kim, *J. Energy Storage*, 2024, **104**, 114584.
33 B. Pourgolmohammad, S. M. Masoudpanah and M. R. Aboutalebi, *Ceram. Int.*, 2017, **43**, 8262–8268.
34 A. Noori, M. F. El-Kady, M. S. Rahmanifar, R. B. Kaner and M. F. Mousavi, *Chem. Soc. Rev.*, 2019, **48**, 1272–1341.
35 Y. Liu, G. Li, L. Huan and S. Cao, *Nanoscale*, 2024, **16**, 504–526.
36 A. Muzaffar, M. B. Ahamed, K. Deshmukh and J. Thirumalai, *Renewable Sustainable Energy Rev.*, 2019, **101**, 123–145.
37 Y. Jiang and J. Liu, *Energy Enivron. Mater.*, 2019, **2**, 30–37.
38 E. Novitskaya, J. P. Kelly, S. Bhaduri and O. A. Graeve, *Int. Mater. Rev.*, 2021, **66**, 188–214.
39 W. Wen and J.-M. Wu, *RSC Adv.*, 2014, **4**, 58090–58100.
40 P. Erri, P. Pranda and A. Varma, *Ind. Eng. Chem. Res.*, 2004, **43**, 3092–3096.
41 B. Pourgolmohammad, S. M. Masoudpanah and M. R. Aboutalebi, *Ceram. Int.*, 2017, **43**, 3797–3803.
42 H. Parnianfar, S. M. Masoudpanah, S. Alamolhoda and H. Fathi, *J. Magn. Magn. Mater.*, 2017, **432**, 24–29.
43 H. Fathi, S. M. Masoudpanah, S. Alamolhoda and H. Parnianfar, *Ceram. Int.*, 2017, **43**, 7448–7453.
44 K. Vijaya Sankar and R. Kalai Selvan, *Electrochim. Acta*, 2016, **213**, 469–481.
45 H. Kennaz, A. Harat, O. Guellati, D. Y. Momodu, F. Barzegar, J. K. Dangbegnon, N. Manyala and M. Guerioune, *J. Solid State Electrochem.*, 2018, **22**, 835–847.
46 B. Rani and N. K. Sahu, *Diamond Relat. Mater.*, 2020, **108**, 107978.
47 T. Huang, Z. Qiu, Z. Hu and X. Lu, *J. Energy Storage*, 2021, **35**, 102286.
48 A. Manohar, T. Suvarna, S. V. Prabhakar Vattikuti, D. Kim, S. Sangaraju, B. A. Al-Asbahi and K. H. Kim, *Inorg. Chem. Commun.*, 2025, **177**, 114393.